CHEMISTRY OF MATERIALS

pubs.acs.org/cm

Article

Miscibility of Li_4GeO_4 into Li_3PS_4 Solid Electrolytes from First-Principles Methods

Yan Li, Zeyu Deng, Chuyang Chen, and Pieremanuele Canepa*

Cite This: https://doi.org/10.1021/acs.chemmater.4c01267

Read Online

ACCESS | Metrics & More | Article Recommendations | Supporting Information

ABSTRACT: Lithium-based oxysulfide solid electrolytes are currently being researched for all-solid-state batteries, as they offer a combination of high electrochemical stabilities and elevated Li-ion conductivities, thus combining the best characteristics of sulfide and oxide solid electrolytes. In this work, we investigated the miscibility of Li_3PS_4 and Li_4GeO_4 polyanions. Building upon a robust multiscale first-principles methodology, we explore the configurational disorder arising from the mixing of GeO_4^{4-} and PS_4^{3-} in the $(1-x)Li_3PS_4-xLi_4GeO_4$ tie line. The computed phase diagram reveals a stable ordered phase with the composition $Li_7PO_4GeS_4$. In $Li_7PO_4GeS_4$, the sulfur atoms initially bound to pentavalent phosphorus as PS_4^{3-} are fully exchanged with oxygen atoms (from GeO_4^{4-}), giving rise to GeS_4^{4-} moieties. *Ab initio* molecular dynamics simulations predicted a high Li-ion conductivity of ~13.31 mS cm^{-1} for $Li_7PO_4GeS_4$ at 573 K. These results reveal the structural complexity and flexibility of these polyanion systems.

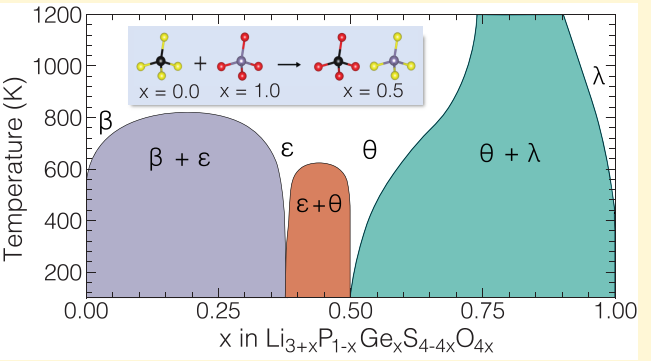

INTRODUCTION

Storing and distributing energy produced by renewable sources, such as solar, wind, and tides, presents a critical challenge in our era. Rechargeable lithium-ion (Li-ion) batteries appear to be the most promising solution to this issue.[1−3] Nevertheless, using flammable, nonaqueous liquid electrolytes in commercial Li-ion cells introduces significant safety concerns. Considerable efforts have been made to advance solid electrolyte (SE) materials for all-solid-state Li-ion batteries. Among inorganic SEs, sulfide, oxide, and halide ceramics[4−6] have received significant scrutiny.

Sulfide SEs are primarily sought after for their high Li ion conductivity (≥10 mS·cm^{-1}) at ambient temperatures,[7,8] along with their compatibility with Li(Na)-S battery architectures.[9,10] However, the susceptibility to moisture and interface instability of sulfide SEs significantly hinder their practical applications.[11−13] Oxide-based SEs generally exhibit a lower Li(Na) ionic conductivity than sulfides. They are recognized for their superior mechanical properties and improved stability at the interface with negative electrode materials.[14] Given these challenges and advantages, oxysulfide SEs have emerged as a potential solution, combining the desirable functional properties of both oxide and sulfide SEs. This statement is supported by various oxysulfide SEs designed by mixing LISICON (an oxide) and thio-LISICON (a sulfide) electrolytes. For example, Takada et al.[15] found that the addition of Li_3PO_4 to Li_3PS_4 results in a new metastable phase ($0.25Li_3PO_4-0.75Li_3PS_4$), which exhibits a conductivity about hundreds of times greater than Li_3PS_4. Enhanced ionic conductivities have also been achieved in the oxysulfide glassy systems by leveraging mixtures of polyanion frameworks, such as $Li_2S-SiS_2-Li_3MO_3$ (with M = B, Al, Ga, and In),[16] $Li_2S-SiS_2-Li_xMO_y$ (M = Si, P, Ge),[17] $xLi_2O-(1-x)(0.6Li_2S-0.4P_2S_5)$,[18] and $70Li_2S\cdot(30-x)P_2S_5\cdot xP_2O_5$.[19] Furthermore, oxygen doping in $Li_{10}GeP_2S_{12}$ (LGPS)[20] has been explored to improve both ionic conductivity and electrochemical stability, as exemplified by $Li_{9.42}Si_{1.02}P_{2.1}S_{9.96}O_{2.04}$,[21] $Li_{3+5x}P_{1-x}S_{4-z}O_z$ ($x = 0.03-0.08$, $z = 0.4-0.8$),[22] $Li_{10}SiP_2S_{12-x}O_x$ ($0 \le x \le 1.75$),[23] $Li_{10}Sn_{0.95}P_2S_{11.9-x}O_x$,[24] and $Li_{10}MP_2S_4O_8$ (M = Si, Ge, Sn).[25] This trend extends to Na-based solid electrolytes, including $Na_3PS_{4-x}O_x$,[26,27] $Na_4P_2S_{7-x}O_x$,[28] and $Na_{2.88}Sb_{0.88}W_{0.12}S_{4-x}O_x$,[29] further highlighting the importance of oxysulfide materials for all-solid-state batteries.

Using advanced computational techniques, this paper explores the pseudobinary oxysulfide system $(1-x)Li_3PS_4-xLi_4GeO_4$. To our knowledge, this specific oxysulfide system remains unexplored experimentally.[15,30−36] Among the parent materials, β-Li_3PS_4, a representative member of the thio-LISICON family, has been extensively studied because of its "simple" crystal structure and high ionic conductivity, reaching

Received: May 3, 2024
Revised: July 30, 2024
Accepted: July 30, 2024

up to 10^{-1} mS·cm^{-1} at room temperature.[37] Meanwhile, Li_4GeO_4, a LISICON-type material, demonstrates versatility in forming diverse solid solution systems with Li_3PO_4[34] and Li_4SiO_4,[38] and has been examined as an additive to enhance the oxidative stability of LLZTO electrolytes to as high as 5.5 V vs Li/Li$^+$.[39]

By mixing different types of polyanions consisting of Ge/P cations and O/S anions, we investigate the existence of potential stable phases within the $Li_{x+3}P_{1-x}Ge_xS_{4-4x}O_{4x}$ tie line. It is anticipated that compounds of this family can provide an optimal balance of electrochemical stability while retaining the elevated ionic conductivity of β-Li_3PS_4. The occurrence of new oxysulfide compounds in the $Li_{x+3}P_{1-x}Ge_xS_{4-4x}O_{4x}$ system is studied by using a multiscale approach, relying on first-principles calculations, cluster expansion, and Monte Carlo simulations. We identified a single stable phase at $x = 0.5$, with the formula $Li_7PO_4GeS_4$.

STRUCTURAL CHARACTERISTICS OF Li_3PS_4 AND Li_4GeO_4

In our pursuit to discover new crystalline compounds with the general formula $Li_{x+3}P_{1-x}Ge_xS_{4-4x}O_{4x}$, it is crucial to examine the structural characteristics of the end members of the oxysulfides, namely, Li_3PS_4 and Li_4GeO_4.

The starting material Li_3PS_4 is known to exist in three phases α, β, and γ, with the γ phase transitioning to the β phase at 573 K, and then to the α phase at 746 K, as detailed by Homma et al.[40] This work focuses on the high-conductivity β form of Li_3PS_4, which crystallizes in an orthorhombic structure with the *Pnma* (No. 62) space group. The experimental structure of β-Li_3PS_4 is shown in Figure S1a. Its conventional unit cell contains four formula units, with three distinct Li sites. Specifically, the Li(1) ions fully occupy the site with Wyckoff multiplicity and label 8*d*, while Li(2) and Li(3) ions partially occupy the 4*b* and 4*c* sites with 70% and 30% occupancy, respectively. The structural optimization using density functional theory (DFT) together with the meta-GGA SCAN functional found the ground state structure of Li_3PS_4 (shown in Figure 1) having 100% occupancy of *d* and *b* type Li sites. Additional exploration of interstitial defects in Li_3PS_4 revealed that the *c*-type site displays the lowest defect energy, which can accommodate extra Li ions. Table S1 summarizes the quantitative comparison between the idealized and experimental structures of Li_3PS_4. Generally, the computed lattice constants of Li_3PS_4 agree well with the experimental measurements within a relative discrepancy of 3%. It is also found that the Li_3PS_4 structure determined using the meta-GGA SCAN functional aligns closely with the local-density approximation results of Lepley et al.[41] In the neutron diffraction structure of β-Li_3PS_4 reported by Kaup et al.[42] the Li1 ions at 8*d* sites split into Li1A and Li1B sites, with partial occupancies of 2/3 and 1/3, respectively. While we used Homma's structure, our model implicitly accounts for this Li-site splitting as our calculations are performed without symmetry constraints. As for the lithium germanate Li_4GeO_4, two structural variations have been reported.[43−45] The high-temperature phase stabilized between 700 and 750 °C is characterized by a monoclinic structure, but details of this structure remain scarce. At ambient temperature, Li_4GeO_4 crystallizes into an orthorhombic structure with space group *Cmcm* (No. 63), as illustrated in Figure S2 and quantified by lattice parameters and atomic positions in Table S2.

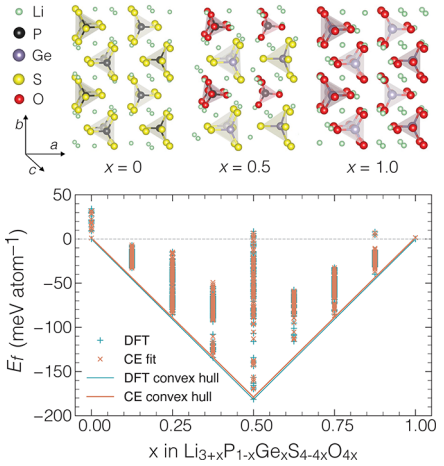

Figure 1. Structural models and predicted phase diagram at 0 K for the $Li_{x+3}P_{1-x}Ge_xS_{4-4x}O_{4x}$ system. The top panel shows in sequence from left to right: structures of *Pnma* Li_3PS_4 at $x = 0$, computationally identified ground state *Pc* $Li_7PO_4GeS_4$ at $x = 0.5$, and *Pnma* Li_4GeO_4 at $x = 1$. Li, P, Ge, S, and O atoms are represented by cyan, black, purple, yellow, and red spheres, respectively. The bottom panel shows the computed formation energy, E_f (defined in eq 1), as a function of composition x. Cyan crosses are DFT simulations, while brown crosses are obtained from cluster expansion (CE) fitting. The phase diagrams at 0 K (illustrated through the convex hull construction) from DFT (cyan line) and CE (brown line) indicate the thermodynamic stability of compositions within the system.

To assess the structural stability of all possible polymorphs of Li_3PS_4 and Li_4GeO_4, we modeled the *Cmcm* and *Pnma* phases for each material. These predicted polymorphs exhibit mild metastability, with the *Cmcm* Li_3PS_4 structure being ∼19.98 meV/atom more unstable than its ground-state *Pnma* phase. Likewise, the *Pnma* Li_4GeO_4 was ∼15.32 meV/atom above the *Cmcm* structure. Details of these predicted phases are summarized in Table S4. While there are no reports of Li_3PS_4 with the *Cmcm* structure, experimental data suggest a hypothetical *Pnma* structure for Li_4GeO_4. This is supported by the work of Rodger et al.[46] on the solid solution system combining Li_4GeO_4 and the *Pnma* phase of γ-Li_3PO_4, which indicates that the extrapolated lattice constants for the pure Ge phase must correspond to a structure isostructural with γ-Li_3PO_4. It is also interesting to mention that a *Pnma* model for Li_4GeO_4 can be theoretically constructed either by substituting O for S in the isostructural Li_4GeS_4 or by replacing PS_4^{3-} units with GeO_4^{4-} and introducing four additional Li ions at the interstitial 4*c* site in Li_3PS_4. Our calculations show that both approaches yield identical optimized structures for Li_4GeO_4, indicating similar crystalline geometry to the *Pnma* (Thio)-LISICON compounds. The optimized *Pnma* structure of Li_4GeO_4 is illustrated in Figures 1 and S3, with details provided in Table S3. Despite Li_4GeO_4 containing more Li ions and larger Ge ions in comparison to Li_3PS_4, the presence of smaller O ions, relative to S ions, leads to a substantial reduction in its lattice volume—approximately 47% smaller than that of Li_3PS_4.

We selected the *Pnma* phase as the host model to investigate the thermodynamic behavior of the $Li_{x+3}P_{1-x}Ge_xS_{4-4x}O_{4x}$ system. The critical difference between Li_3PS_4 and Li_4GeO_4 lies in the atom distribution on the 4*c*-type sites: these sites are unoccupied, acting as the most energetically favorable interstitial sites in Li_3PS_4, but they are filled in Li_4GeO_4.

https://doi.org/10.1021/acs.chemmater.4c01267
Chem. Mater. XXXX, XXX, XXX−XXX

$Li_{x+3}P_{1-x}Ge_xS_{4-4x}O_{4x}$ PHASE BEHAVIOR

A quantitative measure of the thermodynamic mixing of Li_3PS_4 into the Li_4GeO_4 system is obtained by analyzing the enthalpies of mixing, which are approximated by DFT total energies (at 0 K), and thus disregarding the pV term and the zero-point vibrational energy. The formation energy of $Li_{x+3}P_{1-x}Ge_xS_{4-4x}O_{4x}$ at composition x can then be defined as in eq 1:

$$E_f(x) = E(Li_{x+3}P_{1-x}Ge_xS_{4-4x}O_{4x}) - + [(1-x)E(Li_3PS_4) + xE(Li_4GeO_4)] \quad (1)$$

where $E(Li_3PS_4)$ and $E(Li_4GeO_4)$ represent the DFT total energies of the end members Li_3PS_4 and Li_4GeO_4 in the orthorhombic *Pnma* host structure, respectively. The term $E(Li_{x+3}P_{1-x}Ge_xS_{4-4x}O_{4x})$ denotes the DFT-calculated total energy of a specific arrangement (ordering) of Li/Va, P/Ge, and S/O set by composition x.

To explore the compositional landscape of $Li_{x+3}P_{1-x}Ge_xS_{4-4x}O_{4x}$, we examined 1,472 unique orderings at a resolution step of $x = 0.125$. This included the conventional cell (4 formula units with 36 atoms for Li_4GeO_4) and $1 \times 1 \times 2$ supercells of the conventional cell. The DFT formation energies for these structures are shown as cyan crosses in Figure 1. The results reveal that the phase-diagram at 0 K—the convex hull—is formed by three stable structures depicted in the top panel of Figure 1: the two end-members, Li_3PS_4 at $x = 0$ and Li_4GeO_4 at $x = 1.0$, and a newly discovered phase, $Li_7PO_4GeS_4$, at the midpoint $x = 0.5$. Therefore, at 0 K, the intermediate compositions between Li_3PS_4 (Li_4GeO_4) and $Li_7PO_4GeS_4$ will phase separate into a proportional mixture of these stable phases.

Notably, all atoms occupy 2*a*-type sites within the $Li_7PO_4GeS_4$ monoclinic *Pc* (No. 7) structure with two formula units per cell. The computed atomic coordinates of $Li_7PO_4GeS_4$ are shown in Table S5. The lattice constants of $Li_7PO_4GeS_4$ ($a = 11.756$ Å, $b = 7.463$ Å, and $c = 5.791$ Å) lie between those of Li_3PS_4 ($a = 12.979$ Å, $b = 7.994$ Å, and $c = 6.166$ Å) in Table S1 and those of Li_4GeO_4 ($a = 11.254$ Å, $b = 6.184$ Å, and $c = 4.918$ Å) in Table S3.

Upon visual inspection of the $Li_7PO_4GeS_4$ structure (see Figure 1), four key observations can be extracted: (*i*) In the course of the Li_3PS_4 and Li_4GeO_4 mixing, S and O atoms swap their associated cations P and Ge, giving rise to PO_4^{3-} and GeS_4^{4-} tetrahedral moieties. This situation electrostatically stabilizes the structural ordering of Li/Va, P/Ge, and S/O. (*ii*) These tetrahedral moieties do not display anion mixing on P^{5+} or Ge^{4+}, but pristine PO_4^{3-} and GeS_4^{4-} motifs are preferred. (*iii*) The PO_4^{3-} and GeS_4^{4-} units form ordered layers parallel to the (0 1 0) plane, with each GeS_4^{4-} unit attracting an average of four Li ions and each PO_4^{3-} drawing an average of three Li ions in their vicinity. (*iv*) The tetrahedral apexes of both PO_4^{3-} and GeS_4^{4-} in $Li_7PO_4GeS_4$ show alternative upward ($T+$) and downward ($T-$) orientations, which closely resembles the arrangement observed in PS_4^{3-} tetrahedra of *Pnma* Li_3PS_4.

In this work, we denote structural orderings at composition $x = 0.5$ with unique PO_4^{3-} and GeS_4^{4-} motifs as $Li_7PO_4GeS_4$, but compounds of the same compositions are generally represented as $Li_7PGeS_4O_4$. Intuitively, one would expect tetrahedra polyanion units with a mixture of sulfur and oxygen in the form of $GeS_zO_{4-z}^{4-}$ and/or $PS_zO_{4-z}^{3-}$, where $z = 0$, 1, 2, 3, and 4. Intrigued by the question of how the arrangement of tetrahedral moieties influences the structural stabilities of oxysulfides, we categorized the computed $Li_7PGeS_4O_4$ orderings based on the presence of tetrahedra carrying exclusively O or S anions at vertices, here named as "pure" tetrahedra ($z = 0$, 4), or "mixed" ones ($z = 0$, 1, 2) wherein S and O atoms are simultaneously bonded to the same P or Ge. These categories are depicted in Figure 2a. Figure 2b shows the formation

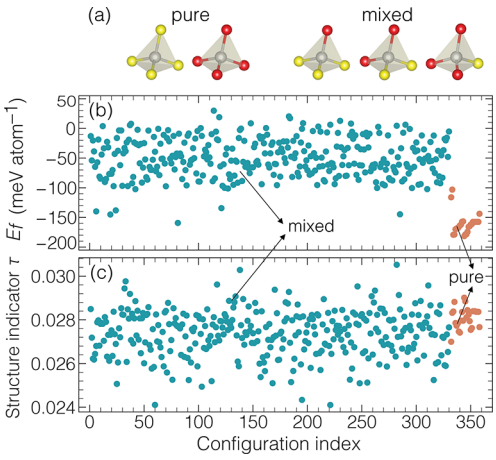

Figure 2. Comparative analysis of tetrahedral moieties in $Li_7PGeS_4O_4$ configurations. (a) Depiction of pure (with all oxygen or sulfur atoms) and mixed tetrahedra. (b) Formation energies and (c) structure indicator τ for configurations featuring either pure (orange markers) or mixed (blue markers) tetrahedra, plotted against an arbitrary configuration index.

energies of 358 unique $Li_7PGeS_4O_4$ orderings (indicated by the configuration index along the x axis), which have been grouped into the pure or mixed tetrahedra. It is apparent from Figure 2b that configurations characterized by pure tetrahedra exhibit more negative formation energies than do most of their mixed counterparts.

Another intriguing aspect concerns whether the chemical character of the tetrahedra affects the accommodation of Li ions in the crystal lattice. This can be preliminarily assessed through a structure indicator $\tau = \sum V_{tetra}/V_{lattice}$, where $\sum V_{tetra}$ represents the volume of the tetrahedra and $V_{lattice}$ is the volume of the model supercell (see Figure 2c). Smaller values of τ suggest a larger free volume for Li ions, and vice versa. While monitoring τ in Figure 2c reveals subtle differences between pure and mixed tetrahedral structures, the minimal variation in values may indicate that this descriptor is not effective in reflecting the chemical character of polyanion units.

We now analyze the role of phonons in the stability of these oxysulfides by investigating the contribution of the vibrational free energy, F_{vib}, to the mixing enthalpy. This analysis also elucidates the dynamical stability of the stable phases within the $Li_{x+3}P_{1-x}Ge_xS_{4-4x}O_{4x}$ system. Phonon calculations at Γ-point were performed using the finite difference approach as implemented in Phonopy.[47]

Changes in vibrational free energy, denoted as $\Delta F_{vib}(x, T)$, are measured relative to the two end members Li_3PS_4 and Li_4GeO_4, using a definition analogous to eq 1. The direct results of ΔF_{vib} were calculated for the lowest-energy $Li_{x+3}P_{1-x}Ge_xS_{4-4x}O_{4x}$ compounds at compositions $x = 0$, 0.25, 0.5, 0.75, and 1 as a function of temperature T from 0 to 1200 K, using $1 \times 2 \times 2$ simulation cells containing 128−144 atoms. Extending to a wider range of compositions, the

https://doi.org/10.1021/acs.chemmater.4c01267
Chem. Mater. XXXX, XXX, XXX−XXX

computed ΔF_{vib} values were subsequently splined over a concentration x and temperature T grid, with increments of $\Delta x = 0.01$ and $\Delta T = 10$ K, respectively.

Figure 3 shows the changes in ΔF_{vib} as a function of x and T. Within $0 \le x \le 1$ and $T \le 350$ K, it is found that the $F_{vib}(x, T)$

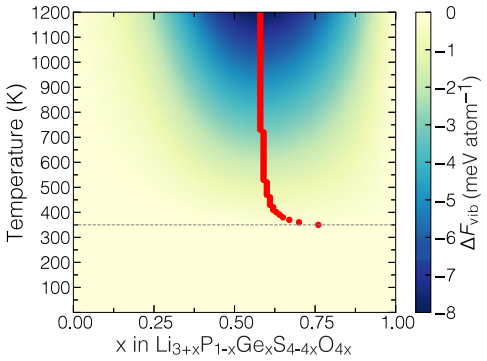

Figure 3. Contour plot of the vibrational free energy difference, ΔF_{vib}, as a function of temperature T and composition x for the $Li_{x+3}P_{1-x}Ge_xS_{4-4x}O_{4x}$ system, interpolated from phonon calculations at specific compositions (see the main text).

values of $Li_{x+3}P_{1-x}Ge_xS_{4-4x}O_{4x}$ are equivalent to the weighted average of the values of Li_3PS_4 and Li_4GeO_4, with ΔF_{vib} vanishing in this region, as demarked by the dashed line in the plot. This implies that the low-temperature ($\le$350 K) mixing enthalpies of $Li_{x+3}P_{1-x}Ge_xS_{4-4x}O_{4x}$ are predominantly determined by the formation energies rather than the vibrational entropy. Above 350 K, Figure 3 illustrates a nearly symmetric distribution of ΔF_{vib} across the composition range of $0.3 \le x \le 0.9$, with minima at specific values of (x, T) marked by red dots. In particular, the location of the ΔF_{vib} minima shifts from $x = 0.76$ at 350 K to $x \sim 0.55$ for temperatures exceeding 440 K.

It is worth noting that the plot of $\Delta F_{vib}(x, T)$ is qualitatively similar to the convex hull of Figure 1. For example, the range of E_f extends from −170.77 meV/atom (at $x = 0.5$) to higher values. In contrast, the minimal $\Delta F_{vib}(x, T)$ is approximately 5% of the lowest E_f in absolute terms, indicating that vibrational contributions have a relatively minor impact on the overall stability of the $Li_{x+3}P_{1-x}Ge_xS_{4-4x}O_{4x}$ compounds. As anticipated, the free energy of mixing of the $Li_{x+3}P_{1-x}Ge_xS_{4-4x}O_{4x}$ system is mostly driven by the formation of stable chemical bonds and electrostatically stable ordering, with an insignificant contribution from vibrational entropy. Analysis of the phonon-band structure of the ground state $Li_7PO_4GeS_4$ (Figure S6) confirms the absence of imaginary phonon frequencies, suggesting that the $Li_7PO_4GeS_4$ structure is dynamically stable.

So far, our analysis suggests an appreciable enthalpic stabilization in the $Li_{x+3}P_{1-x}Ge_xS_{4-4x}O_{4x}$ system from mixing Li_4GeO_4 into Li_3PS_4. This exercise uncovered a stable Li/Va ordering at composition $x = 0.5$, i.e., $Li_7PO_4GeS_4$. We also demonstrated that within the composition range $0.3 \le x \le 0.9$, the vibrational entropy contributions could only mildly affect the miscibility of Li_4GeO_4 and Li_3PS_4. We advance our understanding of the stability of $Li_{x+3}P_{1-x}Ge_xS_{4-4x}O_{4x}$ materials by incorporating configurational entropy effects into the model.

Starting from the formation energies (E_f) of Figure 1, we developed a cluster expansion (CE) model[48,49] trained on 1,021 DFT energies of $Li_{x+3}P_{1-x}Ge_xS_{4-4x}O_{4x}$. The CE model is formulated in terms of effective cluster interactions (ECIs) of pairs, triplets, quadruplets, and higher-order terms, as detailed in the following equation:

$$E_f[\vec{\tau}, \vec{\zeta}, \vec{\kappa}] = V_0 + V_i\tau_i + V_{i,j}\tau_i\tau_j + V_{i,a}\tau_i\zeta_a + V_{a,b}\zeta_a\zeta_b + V_u\kappa_u + V_{u,v}\kappa_u\kappa_v + \cdots \quad (2)$$

Here, $E_f[\vec{\tau}, \vec{\zeta}, \vec{\kappa}]$ represents the formation energy of a configuration, characterized by the occupation vectors $[\vec{\tau}, \vec{\zeta}, \text{and } \vec{\kappa}]$ for Li/Va, Ge/P, and O/S, respectively, at a given composition x. Each ECI includes a polynomial function—τ_i, ζ_a, and κ_u—that maps the occupations of lattice sites with values of ±1 for Li (or its Vacancy), P (or Ge), and S (or O), respectively. The CE in eq 2 is typically truncated, with maximum interaction lengths of 10 Å for pairs, 6 Å for triplets, and 5 Å for quadruplets.

As the Li composition increases along the $Li_{x+3}P_{1-x}Ge_xS_{4-4x}O_{4x}$ tie-line, P^{5+} ions are progressively substituted by Ge^{4+} ions to maintain the stoichiometry and charge neutrality of the system. To accommodate this, we employed the coupled CE formalism developed in ref 50, which, in our system, constrains the concentration ratio of Ge^{4+}/P^{5+} to Li^+/Va by utilizing a common point term, $V_i\phi_i$, in eq 2. Note, the problem does not persist upon the exchange of O^{2-} for S^{2-}, which is described by a separate point term, $V_u\kappa_u$.

The formation energies predicted by the CE model are represented by brown crosses in Figure 1 and agree with the DFT data. The optimized CE incorporates 75 ECI terms, comprising 1 point term, 43 pairs, 27 triplets, and 4 quadruplets (see Table S9 and Figure S8 in Supporting Information), respectively. Quantitatively, the CE model yields a root-mean-square error of ~±4.14 meV/atom and a cross-validation score of ~±3.91 meV/atom. Figure S7 in the Supporting Information displays the energy above the convex hull against the CE model error, defined as the discrepancy between the CE and DFT formation energies.

The fitted CE model was used in semigrand canonical Monte Carlo (SG-CMC) simulations to map the temperature−composition phase diagram of the $Li_{x+3}P_{1-x}Ge_xS_{4-4x}O_{4x}$ system, as in Figure 4. To enforce charge neutrality, the exchange table method was implemented.[50,51] In order to achieve the desired $Li_{x+3}P_{1-x}Ge_xS_{4-4x}O_{4x}$ stoichiometry, one requires that $N^S = 4{\cdot}N^P$ and $N^O = 4{\cdot}N^{Ge}$, with N^i representing the atom count of species i. This necessitates the selection of four S/O atoms (per formula unit) during each SG-CMC sampling event. We adapted the SG-CMC code to meet this requirement, following the flowchart shown in Figure S9 of the Supporting Information. Details regarding simulation cell size, chemical potential μ, and phase boundary analysis are in the SI.

In Figure 4, four distinct single-phase regions are identified and labeled as β, ϵ, θ, and λ. The β phase corresponds to Li_3PS_4, and the λ phase corresponds to Li_4GeO_4. Figure 4 reveals the ϵ phase located at $x = 0.375$, which appears stable at a low temperature ~100 K. The θ phase at $x = 0.5$ is associated with Pc $Li_7PO_4GeS_4$. Biphasic regions and domes are represented by colored shapes separating the single-phase regions. The two-phase regions identified are (*i*) $\beta + \epsilon$ (violet dome), existing in the composition range of $0 < x < 0.375$ and below 825 K; (*ii*) $\epsilon + \theta$ (orange dome), spanning the composition range of $0.375 < x < 0.5$ and temperature lower than ~624 K; and (*iii*) a biphasic region $\theta + \lambda$ (aqua shape)

https://doi.org/10.1021/acs.chemmater.4c01267
Chem. Mater. XXXX, XXX, XXX−XXX

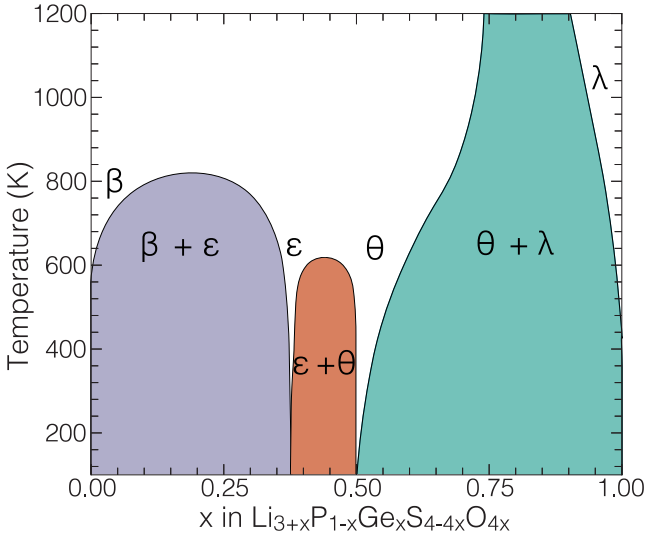

Figure 4. Predicted temperature−composition phase diagram for the $Li_{x+3}P_{1-x}Ge_xS_{4-4x}O_{4x}$ system, derived from SG-CMC simulations based on the CE model.

dominating a substantial range of compositions $0.5 < x < 1.0$ and temperatures.

The single-phase Li-rich region—the λ phase—extends over a narrow composition range and is observed at temperatures > 480 K. Below that temperature and at $x = 1$, the λ phase retains the characteristics of Li_4GeO_4. In contrast, the Li, Ge, and O solubilities into the β phase (Li_3PS_4) appear much more pronounced. The θ phase, corresponding to the *Pc* $Li_7PO_4GeS_4$ compound at $x = 0.5$, exhibits remarkable stability over a substantial temperature range. As the temperature increases, Li, Ge, and O solubility increases in the θ phase, eventually leading to a fully mixed phase region of $\theta + \lambda$ at high temperatures. Above 825 K, the β, ϵ, and θ phases merge into a disordered single-phase region with significant Li, Ge, and O solubility.

Figure 5b plots the variation of configurational entropy S_{config} with composition x at temperatures $T = 300$, 500, and 800 K, respectively. Results are compared with the vibrational entropy

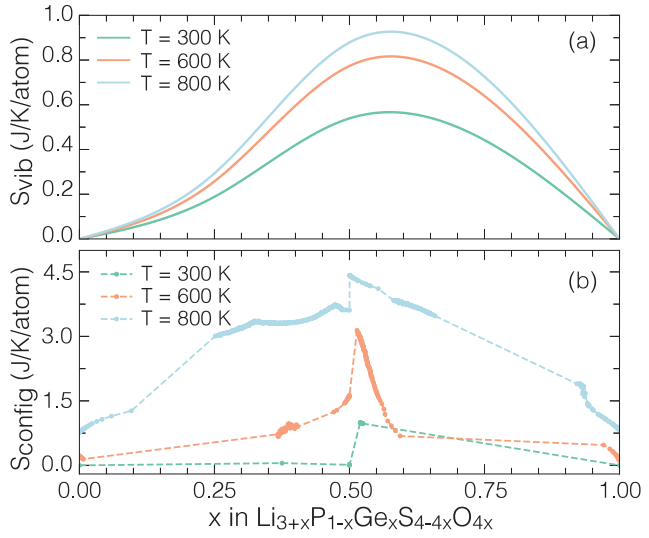

Figure 5. (a) Vibrational entropy S_{vib} and (b) configurational entropy S_{config} at selected temperatures of 300, 600, and 800 K.

S_{vib}, which has a milder contribution compared to S_{config}, particularly at high temperatures >600 K. At $T = 300$ K, S_{config} shows minima at $x = 0$, 0.375, 0.5, 1.0, consistent with the single-phase regions observed in the phase diagram of Figure 4. With an increase in temperature, S_{config} increases especially at $x = \sim 0.5$, suggesting a higher degree of configurational disorder or enhanced mixing in that region.

ELECTROCHEMICAL STABILITY OF $Li_{x+3}P_{1-x}Ge_xS_{4-4x}O_{4x}$

Understanding the oxygen solubility in Li_3PS_4 is primarily aimed at expanding the electrochemical stability windows of these solid electrolyte (SE) materials. To predict the stability windows, we constructed a grand-potential phase diagram in the Li−P−Ge−S−O composition space, following previous studies.[52−55] Polymorphs for all known elements and binary, ternary, quaternary, and quintenary compounds within this space were computed using starting structures from the Inorganic Crystal Structure Database.[56] The Li−P−Ge−S−O phase diagram was further enriched by incorporating the $Li_{x+3}P_{1-x}Ge_xS_{4-4x}O_{4x}$ structures of Figure 1.

From the perspective of thermodynamic equilibrium, the electrochemical stability window of an SE is determined by the range of the Li chemical potential μ_{Li} within which the SE material remains stable against electrochemical transformations at electrode interfaces during cycling. Given a compound of interest, e.g., $Li_{x+3}P_{1-x}Ge_xS_{4-4x}O_{4x}$, open to a Li reservoir, the relevant energy descriptor is the grand potential thermodynamic function, $\Phi(\text{compound}, \mu_{Li}) = G(\text{compound}) - n_{Li}[\text{compound}]\ \mu_{Li}$. Here, G(compound) is the Gibbs free energy of the compound approximated by the DFT total energy E(compound), and n_{Li}[compound] is the number of Li atoms within the compound. By adjustment of μ_{Li} in a suitable range, the stable compounds can be identified by computing the lower envelope of the grand-potential Φ (compound, μ_{Li}) function. At a given μ_{Li}, it is convenient to define the grand-potential energy difference, ΔE_d, between the compound investigated and its phase equilibria, resulting in $\Delta E_d(\text{compound}, \mu_{Li}) = [\Phi(\text{equilibria}, \mu_{Li}) - \Phi(\text{compound}, \mu_{Li})]/N_{non-Li}$, where N_{non-Li} is the number of nonlithium atoms in the compound.

Considering Li/Li^+ as the reference electrode, μ_{Li} directly correlates with the voltage according to $\phi = -\frac{\mu_{Li}}{zF}$ in Volts (V), where z is the number of electrons transferred, F is the Faraday constant, and μ_{Li} is referenced to the chemical potential of Li metal. By definition, a stable SE resists both Li extraction (oxidation at high voltage/low potential) and Li insertion (reduction at low voltage/high potential) within its stability window. Ideally, good electrolytes should demonstrate a cathodic stability limit as close as possible to $\phi_{CL} = 0.0$ V vs Li/Li^+ when in contact with a negative electrode material, and an anodic stability limit $\phi_{AL} > 4.5$ V vs Li/Li^+ against the positive electrode material. The voltage range between the cathodic and anodic limits sets the stability window of the SEs.

The electrochemical stability windows for several compounds are shown in Figure 6. Detailed reaction equations at critical voltages can be found in Table S10 of the Supporting Information. As expected, the oxide-based materials, Li_4GeO_4 and Li_3PO_4, have significantly wider electrochemical stability windows (2.28 and 3.57 V vs Li/Li^+) in comparison to their sulfide counterparts, Li_4GeS_4 (~0.59 V) and Li_3PS_4 (~0.43 V). The $Li_7PO_4GeS_4$ identified at composition $x = 0.5$ exhibits a

https://doi.org/10.1021/acs.chemmater.4c01267
Chem. Mater. XXXX, XXX, XXX−XXX

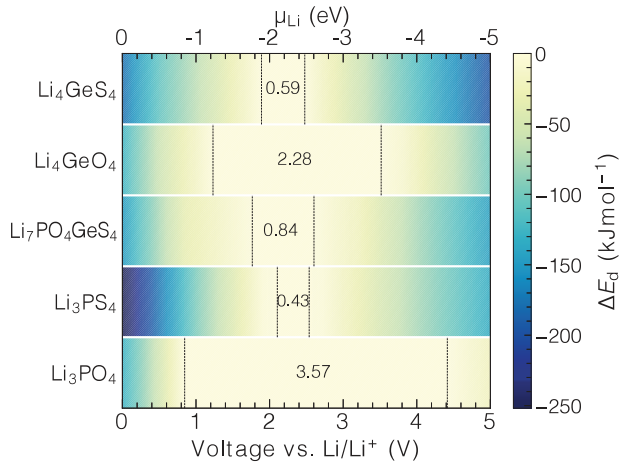

Figure 6. Electrochemical stability windows for Li_4GeS_4, Li_4GeO_4, $Li_7PO_4GeS_4$, Li_4PS_4, and Li_3PO_4. The color bar indicates the magnitude of the decomposition reactions ΔE_d expressed in kJ mol^{-1}. The left and right vertical dashed lines within each bar denote the cathodic limit (reduction potential) and anodic limit (oxidation potential).

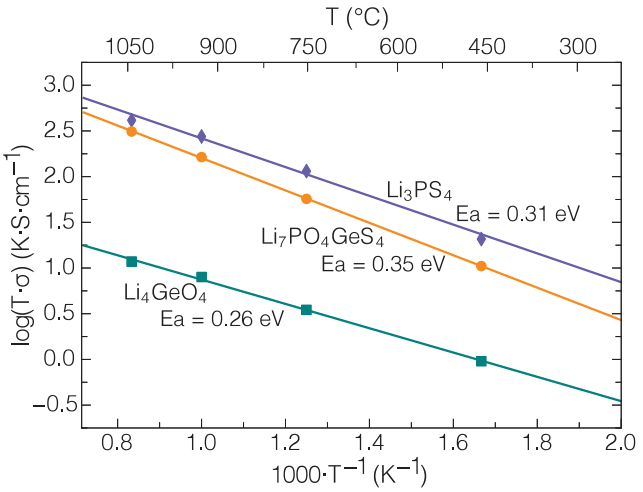

Figure 7. Plots of the simulated ionic conductivity of Li_3PS_4 (purple), $Li_7PO_4GeS_4$ (orange), and Li_4GeO_4 (green). The lines represent the best linear fit to the calculated data.

stability window of ~0.84 V vs Li/Li^+, which is more than ~0.4 V higher than Li_3PS_4.

As illustrated in Figure 6, the cathodic limits $\phi_{CL}(Li_3PS_4) \sim 2.105 > \phi_{CL}(Li_7GePS_4O_4) \sim 1.765 > \phi_{CL}(Li_4GeO_4) \sim 1.231$ V vs Li/Li^+, whereas a reverse trend is observed for the anodic limit ϕ_{AL}, which is 2.538 < 2.603 < 3.516 V vs Li/Li^+, for Li_3PS_4, $Li_7PO_4GeS_4$, and Li_4GeO_4, respectively. Given that half of the tetrahedra in the $Li_7PO_4GeS_4$ structure are PO_4^{3-} ions, the robust P−O bonds coupled with the higher electronegativity of oxygen likely impart stability of this SE at lower voltages or higher voltages compared to Li_3PS_4. However, Ge is more readily reduced than P under similar conditions. This fact is supported by the low standard reduction potentials for Ge $E°$ ($Ge^{4+} + 4e^- \rightarrow Ge$) ≈ 0.124 V vs SHE.[57] The wider stability window of ~3.57 V vs Li/Li^+ for Li_3PO_4 compared to 2.28 V for Li_4GeO_4 supports this observation. Therefore, substituting P^{5+} with Ge^{4+} will reduce the stability window of compounds along the $Li_{x+3}P_{1-x}Ge_xS_{4-4x}O_{4x}$ tie-line. This could explain why the window width of $Li_7PO_4GeS_4$ (0.84 V vs Li/Li^+) does not show a pronounced enhancement, falling in between Li_3PS_4 (0.43 V) and Li_4GeO_4 (2.28 V).

■ Li^+ MOBILITY IN $Li_{x+3}P_{1-x}Ge_xS_{4-4x}O_{4x}$

To assess Li-ion diffusion in $Li_7PO_4GeS_4$ and understand its connection to its parent phases, Li_3PS_4 and Li_4GeO_4, we conducted *ab initio* molecular dynamics (AIMD) simulations. Computed Arrhenius plots of Li-ion conductivities vs inverse of temperature are shown in Figure 7.

Across the temperature explored, the computed Li-ion conductivities follow the order $Li_4GeO_4 \ll Li_7PO_4GeS_4 < Li_3PS_4$. With a substantial ionic conductivity of ~30.76 mS cm^{-1} at 573 K (~300 °C), the extrapolated activation energy of ~0.31 eV of β-Li_3PS_4 appears in agreement with previous reports as 0.20−0.50 eV.[41,58,59] In the absence of experimental data for comparison to the *Pnma* Li_4GeO_4 phase, we computed an activation energy of ~0.26 eV and conductivity of 1.33 mS cm^{-1} at 573 K. Although $Li_7PO_4GeS_4$ displays a modest activation energy (0.35 eV), its ionic conductivity at 573 K is approximately 1 order of magnitude higher (13.31 mS cm^{-1}) compared to that of Li_4GeO_4.

Li-ion trajectories of Figure S10, shown as a superposition of MD snapshots, reveal appreciable Li-ion mobility in all three materials. While the precise sequence of individual ion displacement is not reported, it is evident that Li-ion diffusion in the *Pnma* structure primarily occurs along migration pathways formed by the 8*d*, 4*c*, and 4*d* sites. Notably, for all materials, the most frequent Li-ion conduction pathways reside within the *ac* plane (bottom panel of Figure S10), consistent with prior findings of low migration barriers along the *a* and *c* axes in β-Li_3PS_4.[41] Comparing the Li-ion trajectories along the *c* axis (top panel in Figure S10) in Li_3PS_4 and $Li_7PO_4GeS_4$ demonstrates qualitatively similar spatial distributions. However, as highlighted in Figure S10, Li-ion trajectories in Li_3PS_4 predominantly follow "straight" paths between the homogeneous PS_4^{3-} layers, whereas Li-diffusion channels in $Li_7PO_4GeS_4$ appear more tortuous because of the alternating environment set by ordered arrangements of PO_4^{3-} and GeS_4^{4-} tetrahedra. Qualitatively, this may explain the reduced Li-ion conductivity in $Li_7PO_4GeS_4$ compared to Li_3PS_4. The analysis also reveals that Li ions preferentially "agglomerate" closer to the GeS_4^{4-} groups compared to PO_4^{3-}, with each S atom coordinated by ~1.34 Li ions and each oxygen atom by ~0.82 Li ions, respectively. In Li_4GeO_4, Li-ion trajectories are predominantly confined to localized regions, suggesting constrained Li diffusion due to narrow migration channels between GeO_4^{4-} blocks.

■ DISCUSSION

Oxysulfide SEs represent a promising class of materials for all-solid-state batteries, integrating the merits of oxide and sulfide SEs to achieve the desired electrolyte performance. The theoretical design of oxysulfide SEs typically involves partially substituting oxygen (O) atoms within known sulfide (S)-based SE frameworks. However, the triple atomic substitutions, as seen in the $Li_{x+3}P_{1-x}Ge_xS_{4-4x}O_{4x}$ system entailing Li/Va, Ge/P, and O/S exchanges, undoubtedly present a significant leap in complexity in material design.

Due to the high configurational degrees of freedom of the $Li_{x+3}P_{1-x}Ge_xS_{4-4x}O_{4x}$ system, many symmetrically inequivalent atomic orderings emerge at intermediate compositions. This study developed an extended Ising Hamiltonian, as imple-

https://doi.org/10.1021/acs.chemmater.4c01267
Chem. Mater. XXXX, XXX, XXX−XXX

mented in the cluster expansion model, to find possible stable phases along the $Li_{x+3}P_{1-x}Ge_xS_{4-4x}O_{4x}$ tie-line.

The new stable phase $Li_7PO_4GeS_4$ identified along the $Li_{x+3}P_{1-x}Ge_xS_{4-4x}O_{4x}$ tie-line at composition $x = 0.5$ (see Figure 1) is characterized by a framework of equimolar PO_4^{3-} and GeS_4^{4-} tetrahedral moieties forming regular geometric patterns. Surprisingly, $Li_7PO_4GeS_4$ encompasses the exchange of cations; S atoms from Li_3PS_4 and O atoms from Li_4GeO_4 are swapped between P and Ge cations. The thermodynamic stability of the $Li_7PO_4GeS_4$ phase over a wide range of temperatures was further confirmed by the predicted phase diagram of Figure 4. However, if synthesizable, the formation of mixed tetrahedral polyanions in $Li_7PGeS_4O_4$ cannot be definitively ruled out, particularly under high-temperature synthesis conditions. The phase diagram also indicates that, at $T > 825$ K, the three single phases, β, ϵ, and θ, will mix through an order−disorder phase transition into a disordered single phase. Beyond 1200 K, it is plausible to expect a progressive narrowing of the biphasic region until the $\theta + \lambda$ phase boundary closes, resulting in the confluence of all four single phases (β, ϵ, θ, and λ) into a single disorder phase. These findings imply that high-temperature synthesis might facilitate the incorporation of Li, Ge, and O atoms into Li_3PS_4. Furthermore, fast quenching of high-temperature phases may preserve the materials in a disordered single phase with potentially higher ionic conductivities than highly ordered phases.

Progressing from Li_3PS_4 to $Li_7PO_4GeS_4$ and to Li_4GeO_4, the interplay between sulfur-to-oxygen and phosphorus-to-germanium substitutions reveals intricate effects of the electrochemical stability of these SEs. Indeed, the partial substitution of S with O from Li_3PS_4 (0.43 V vs Li/Li^+) to $Li_7PO_4GeS_4$ (0.84 V vs Li/Li^+) props open the stability window by over 0.4 V. This enhancement can likely be attributed to the higher electronegativity of O atoms and stronger P−O bonds. Nonetheless, given the lower reduction potential of Ge compared to P, the stability window $Li_7PO_4GeS_4$ is not significantly enhanced compared to 2.28 V vs Li/Li^+ for Li_4GeO_4. Therefore, the computed intermediate values for the stability window of $Li_7PO_4GeS_4$ reflect the combined effects of S and O substitutions and Ge substitutions.

To further investigate the arrangement of tetrahedra species, PO_4^{3-} + GeS_4^{4-}, in β-$Li_7PO_4GeS_4$ (obtained from β-Li_3PS_4), we extended our investigation to an ordered γ-$Li_7PGeS_4O_4$ obtained from the $Pmn2_1$ γ-Li_3PS_4 structure. From the analysis of the 140 distinct configurations, we identified the lowest-energy γ-$Li_7PO_4GeS_4$ structure (Figure S4b) that is characterized by a $P1$ symmetry and lies ∼1.89 meV/atom higher than its β-$Li_7PO_4GeS_4$ analogue. Similarly to β-$Li_7PO_4GeS_4$, the γ variant also includes pure PO_4^{3-} and GeS_4^{4-} tetrahedra moieties. The orientation of all the tetrahedral apexes in γ-Li_3PS_4 is uniformly $T+$ (see Figure S4a), whereas in γ-$Li_7PO_4GeS_4$ all GeS_4^{4-} tetrahedra orient as $T+$, and all PO_4^{3-} are $T-$. This difference can be linked to the substitution of S^{2-} with O^{2-} in γ-Li_3PS_4, where oxygen anions form shorter and stronger bonds with P^{5+} than sulfur and likely alter the spatial configuration of the PO_4^{3-} tetrahedra compared to that of GeS_4^{4-}. The role of tetrahedral orientation and dynamics on Li ion diffusion may be inferred from previous studies for the β and γ polymorphs of Li_3PS_4.[59,60] However, the impact of these factors on the β and γ $Li_7PO_4GeS_4$ structures is currently elusive.

It is important to compare $Li_7PGeS_4O_4$, templated on the LGPS-type Li_7GePS_8 SE material,[20,61] with the β-$Li_7PO_4GeS_4$ structure identified in this study. The experimental structure of Li_7GePS_8 exhibits tetragonal $P4_2/nmc$ symmetry with atomic positions similar to those in LGPS. Upon analyzing 150 unique $Li_7PGeS_4O_4$ orderings modeled on the Li_7GePS_8 structure, we found that the lowest-energy LGPS-$Li_7PO_4GeS_4$ is ∼7 meV/atom higher in energy compared to its β-$Li_7PO_4GeS_4$ analogue. Pure PO_4^{3-} and GeS_4^{4-} tetrahedral units are recurrent in the LGPS-$Li_7PO_4GeS_4$ structure (Figure S5), with all tetrahedra apexes uniformly oriented within the structure. While it is not yet clear whether LGPS-$Li_7PO_4GeS_4$ retains the high ionic conductivity of Li_7GePS_8 (∼10 $mS{\cdot}cm^{-1}$),[61] so far, results suggest that controlling the processing conditions that favor specific tetrahedral orientations may improve the stability or ionic conductivities of the resulting $Li_7PO_4GeS_4$ SE.

In the stable structures of $Li_7PGeS_4O_4$, templated on β and γ-Li_3PS_4, and the LGPS-type Li_7GePS_8 phases, there is a consistent preference of pure PO_4^{3-} and GeS_4^{4-} tetrahedra over the occurrence of mixed O^{2-} and S^{2-} moieties. Indeed, homogeneous PO_4^{3-} and GeS_4^{4-} tetrahedra units are highly symmetric compared with mixed moieties, thereby minimizing the lattice strain of the system. Speculatively, mixed tetrahedra that combine fractions of the O and S anions on the same cations could increase the vibrational entropy of the system, facilitating the miscibility of Li_3PS_4 and Li_4GeO_4 at high temperatures and potentially lowering the temperatures of phase transitions. Our calculations also demonstrate the strong electrostatic stabilization imparted by forming pure tetrahedra moieties, which results in a remarkable enthalpic stabilization of lower-energy orderings (see Figure 1).

Furthermore, O atoms tend to favor P^{5+} centers over Ge^{4+} cations due to the stronger P−O covalent bonds than P−S. This hypothesis is supported by the favorable reaction $Li_4GeO_4 + Li_4PS_4 \rightarrow Li_4GeS_4 + Li_4PO_4$ −20.26 kJ mol^{-1} (where each structure is in the *Pnma* symmetry). The interplay between the distribution of Li ions and polyanion tetrahedra, not examined here, could also influence the overall stability of the $Li_7PGeS_4O_4$ structure. However, the recurrent presence of pure PO_4^{3-} and GeS_4^{4-} tetrahedral moieties in those low-energy $Li_7PO_4GeS_4$ structures provides electrostatic stabilization of these mixed P/Ge and O/S phases.

The ionic conductivity of $Li_7PO_4GeS_4$ shows a consistent increase compared to Li_4GeO_4, specifically ∼10 times higher at 573 K. This enhancement is likely attributed to the half substitution of the more polarizable and larger S^{2-} anions, which weakens Li−S bonding and expands the Li-ion diffusion pathways, thus facilitating Li ion mobility within the spaces formed by the ordered PO_4^{3-} and GeS_4^{4-} tetrahedra framework. Furthermore, as shown in Figure 7, the ionic conductivity of $Li_7PO_4GeS_4$ converges toward that of Li_3PS_4 at elevated temperatures. This possibly suggests that the influence of the mixed anion (PO_4^{3-} and GeS_4^{4-}) sublattice on Li-ion mobility in $Li_7PO_4GeS_4$ is mitigated at higher temperatures due to increased thermal energy, which may overcome the differences in local bonding environments.

CONCLUSION

In summary, this study provided a comprehensive thermodynamic investigation of the mixing of phosphate and the thiophosphate polyanion in $Li_{x+3}P_{1-x}Ge_xS_{4-4x}O_{4x}$ solid electrolytes. The model builds upon a robust multiscale approach based on first-principles calculations, a complex coupled-

https://doi.org/10.1021/acs.chemmater.4c01267
Chem. Mater. XXXX, XXX, XXX−XXX

cluster expansion framework, and large-size Monte Carlo simulations, thus capturing the configurational disorder of GeO_4^{4-} and PS_4^{3-} mixing. The interplay of vibrational and configurational entropy terms on the mixing of these polyanion systems was considered explicitly, demonstrating that phonon contributions have only a minor effect on the solubility of PS_4^{3-} in GeO_4^{4-}. In the $Li_{x+3}P_{1-x}Ge_xS_{4-4x}O_{4x}$ tie-line, we identified a new thermodynamically and dynamically stable mixed phase $Li_7PO_4GeS_4$. Surprisingly, $Li_7PO_4GeS_4$ displays GeS_4^{4-} and PO_4^{3-} tetrahedra formed by an exchange of sulfur atoms—initially bound to pentavalent phosphorus in PS_4^{3-} units—with oxygen atoms from the GeO_4^{4-} groups. In $Li_7PO_4GeS_4$, PO_4^{3-} and GeS_4^{4-} tetrahedral moieties order, forming regular geometric patterns. The electrochemical stability windows of $Li_7PO_4GeS_4$ (0.84 V vs Li/Li^+) lie in between Li_3PS_4 (0.43 V) and Li_4GeO_4 (2.28 V). The mild increase in the stability window of $Li_7PO_4GeS_4$ compared to Li_4GeO_4 was associated with the facile reduction of Ge^{4+} to metallic Ge. First-principles molecular dynamics simulations reveal a clear trend in Li-ion conductivity: Li_3PS_4 > $Li_7PO_4GeS_4$ > Li_4GeO_4. This highlights the influence of anion composition and structure on Li-ion transport, with the oxysulfide $Li_7PO_4GeS_4$ offering a promising compromise between the sulfide's high conductivity and the oxide's stability. The results of this investigation highlight the structural complexity of the phase space of polyanion systems for lithium and sodium solid electrolytes, which deserves more experimental and theoretical investigations.

METHODS

Calculations of this investigation were based on density-functional theory (DFT),[62] as implemented in the Vienna Ab initio Simulation Package (VASP).[63,64] The core electrons were described using the projector augmented wave (PAW) formalism.[65] The "Strongly Constrained and Appropriately Normed Semilocal Density Functional" (SCAN) meta-GGA semilocal functional was employed to approximate the exchange and correlation functional in DFT.[66] In contrast to generalized-gradient approximation functionals, the SCAN functional addresses the issue of overbinding in the O_2 and S_2 molecules, thereby providing more accurate formation energies for oxides and sulfides. The PAW potentials used include: `Li_sv 10Sep2004` $1s^22s^1$, `P 06Sep2000` $3s^23p^3$, `Ge_d03Jul2007` $3d^{10}4s^24p^2$, `S 06Sep2000` $3s^23p^4$, and `O 08Apr2002` $2s^22p^4$.

This investigation starts with the construction of a set of crystalline compounds with the general formula $Li_{x+3}P_{1-x}Ge_xS_{4-4x}O_{4x}$, where x = 0 and 1 correspond to the end-member compositions, i.e., Li_3PS_4 and Li_4GeO_4. Intermediate compositions were explored by setting an interval of Δx = 0.125. As the composition x decreases along the $Li_{x+3}P_{1-x}Ge_xS_{4-4x}O_{4x}$ tie line, Li vacancies are introduced as Ge^{IV} atoms are progressively replaced by pentavalent P^V atoms, leading to configurations with various arrangements (orderings) of Li/Vacancies(Va), Ge/P, and S/O. The sheer number of possible orderings in the $Li_{x+3}P_{1-x}Ge_xS_{4-4x}O_{4x}$ system is managed with the Python library Pymatgen.[67] The classical Ewald energy of unrelaxed configurations was computed by assigning formal charges to each atomic species (Li^{1+}; Ge^{4+} and P^{5+}; and S^{2-} and O^{2-}, respectively). This approach identified 1,472 representative initial configurations with relatively "low" classical Ewald energies. The total number of unique $Li_{x+3}P_{1-x}Ge_xS_{4-4x}O_{4x}$ configurations over the whole composition range was further reduced to 1,021 after eliminating symmetrical equivalent structures. The DFT total energies for these geometrically optimized (atomic positions, cell shape, and volume) orderings were obtained by using plane-wave expansions up to an energy cutoff of 520 eV. The first Brillouin zone was integrated by using a Γ-centered Monkhorst–Pack homogeneous sampling with a step of 0.5 $Å^{-1}$ (or smaller) in each lattice direction. The convergence threshold for changes in the DFT total energy was set to 10^{-5} eV/cell. Forces on the atoms were considered converged within 10^{-2} eV/Å.

To simulate the Li-ion migration, *ab initio* molecular dynamics (AIMD) calculations were performed in canonical NVT ensemble enabled by a Nosé–Hoover thermostat.[68,69] 1 × 2 × 2 supercells were constructed by expanding the conventional cells of Li_3PS_4, $Li_7PO_4GeS_4$, and Li_4GeO_4, containing 128, 136, and 144 atoms, respectively. To reduce computational costs, the generalized gradient approximation (GGA) by Perdew, Burke, and Ernzerhof[70] was employed as the exchange-correlation functional, the energy cutoff was reduced to 420 eV, and the total energy was integrated at the Γ point. Simulations were conducted at 600, 800, 1000, and 1200 K temperatures with an integration step of 1 fs and simulations times longer than 100 ps at each temperature.

ASSOCIATED CONTENT

Supporting Information

The Supporting Information is available free of charge at https://pubs.acs.org/doi/10.1021/acs.chemmater.4c01267.

Calculated lattice parameters for all structures, details regarding the cluster expansion and Monte Carlo simulations, information on free energy integration, phonon dispersion curves, and details of the *ab initio* molecular dynamics simulations (PDF)

AUTHOR INFORMATION

Corresponding Author

Pieremanuele Canepa − *Department of Electrical and Computer Engineering and Texas Center for Superconductivity, University of Houston, Houston, Texas 77204, United States; Department of Materials Science and Engineering, National University of Singapore, 117575, Singapore;* orcid.org/0000-0002-5168-9253; Email: pcanepa@uh.edu

Authors

Yan Li − *Department of Materials Science and Engineering, National University of Singapore, 117575, Singapore*

Zeyu Deng − *Department of Materials Science and Engineering, National University of Singapore, 117575, Singapore;* orcid.org/0000-0003-0109-9367

Chuyang Chen − *Department of Materials Science and Engineering, National University of Singapore, 117575, Singapore*

Complete contact information is available at: https://pubs.acs.org/10.1021/acs.chemmater.4c01267

Notes

The authors declare no competing financial interest.

ACKNOWLEDGMENTS

P.C. acknowledges funding from the National Research Foundation under his NRF Fellowship NRFF12-2020-0012, Singapore. P.C. acknowledges a Robert Welch professorship at the Texas Center for Superconductivity. Z.D. acknowledges the support from his Lee Kuan Yew Postdoctoral Fellowship 22-5930-A0001 and the Ministry of Education, Singapore, under the Academic Research Fund Tier 1 (FY2024). The computational work was performed on resources of the National Supercomputing Centre, Singapore (https://www.nscc.sg). This work also used the computational resources of the supercomputer Fugaku provided by the RIKEN Centre for Computational Science under the "Fugaku Projects via

National Supercomputing Centre Singapore" and through the HPCI System Research Project (Project ID: hp230188).

REFERENCES

(1) Goodenough, J. B.; Park, K.-S. The Li-ion rechargeable battery: a perspective. *J. Am. Chem. Soc.* **2013**, *135*, 1167−1176.

(2) Nitta, N.; Wu, F.; Lee, J. T.; Yushin, G. Li-ion battery materials: present and future. *Mater. Today* **2015**, *18*, 252−264.

(3) Li, M.; Lu, J.; Chen, Z.; Amine, K. 30 years of lithium-ion batteries. *Adv. Mater.* **2018**, *30*, 1800561.

(4) Quartarone, E.; Mustarelli, P. Electrolytes for solid-state lithium rechargeable batteries: recent advances and perspectives. *Chem. Soc. Rev.* **2011**, *40*, 2525−2540.

(5) Ye, T.; Li, L.; Zhang, Y. Recent progress in solid electrolytes for energy storage devices. *Adv. Funct. Mater.* **2020**, *30*, 2000077.

(6) Tan, S.-J.; Zeng, X.-X.; Ma, Q.; Wu, X.-W.; Guo, Y.-G. Recent advancements in polymer-based composite electrolytes for rechargeable lithium batteries. *Electrochemical Energy Reviews* **2018**, *1*, 113−138.

(7) Kato, Y.; Hori, S.; Saito, T.; Suzuki, K.; Hirayama, M.; Mitsui, A.; Yonemura, M.; Iba, H.; Kanno, R. High-power all-solid-state batteries using sulfide superionic conductors. *Nature Energy* **2016**, *1*, 16030.

(8) Li, Y.; Song, S.; Kim, H.; Nomoto, K.; Kim, H.; Sun, X.; Hori, S.; Suzuki, K.; Matsui, N.; Hirayama, M.; et al. others A lithium superionic conductor for millimeter-thick battery electrode. *Science* **2023**, *381*, 50−53.

(9) Sakuda, A.; Hayashi, A.; Tatsumisago, M. Sulfide solid electrolyte with favorable mechanical property for all-solid-state lithium battery. *Sci. Rep.* **2013**, *3*, 2261.

(10) Wu, J.; Liu, S.; Han, F.; Yao, X.; Wang, C. Lithium/sulfide all-solid-state batteries using sulfide electrolytes. *Adv. Mater.* **2021**, *33*, 2000751.

(11) Zhu, Y.; Mo, Y. Materials design principles for air-stable lithium/sodium solid electrolytes. *Angew. Chem., Int. Ed.* **2020**, *59*, 17472−17476.

(12) Lu, P.; Wu, D.; Chen, L.; Li, H.; Wu, F. Air stability of solid-state sulfide batteries and electrolytes. *Electrochemical Energy Reviews* **2022**, *5*, 3.

(13) Yersak, T. A.; Zhang, Y.; Hao, F.; Cai, M. Moisture Stability of Sulfide Solid-State Electrolytes. *Frontiers in Energy Research* **2022**, *10*, 882508.

(14) Deng, Z.; Mishra, T. P.; Mahayoni, E.; Ma, Q.; Tieu, A. J. K.; Guillon, O.; Chotard, J.-N.; Seznec, V.; Cheetham, A. K.; Masquelier, C.; et al. Fundamental investigations on the sodium-ion transport properties of mixed polyanion solid-state battery electrolytes. *Nat. Commun.* **2022**, *13*, 4470.

(15) Takada, K.; Osada, M.; Ohta, N.; Inada, T.; Kajiyama, A.; Sasaki, H.; Kondo, S.; Watanabe, M.; Sasaki, T. Lithium Ion Conductive Oxysulfide, Li_3PO_4−Li_3PS_4. *Solid State Ionics* **2005**, *176*, 2355−2359.

(16) Hayashi, A.; Komiya, R.; Tatsumisago, M.; Minami, T. Characterization of Li_2S−SiS_2−Li_3MO_3 (M = B, Al, Ga and In) Oxysulfide Glasses and Their Application to Solid State Lithium Secondary Batteries. *Solid State Ionics* **2002**, *152*−*153*, 285−290.

(17) Hayashi, A.; Yamashita, H.; Tatsumisago, M.; Minami, T. Characterization of Li_2S−SiS_2−Li_xMO_y (M = Si, P, Ge) Amorphous Solid Electrolytes Prepared by Melt-Quenching and Mechanical Milling. *Solid State Ionics* **2002**, *148*, 381−389.

(18) Rao, R. P.; Seshasayee, M. Oxysulfide Glasses xLi_2O−$(1-x)(0.6Li_2S$−$0.4P_2S_5)$. *J. Power Sources* **2006**, *159*, 258−262.

(19) Gonzalez Malabet, H. J.; Zhang, Y.; Salvador, J. R.; Schmidt, R. D.; Yersak, T. A. Improved Thermal Stability of Oxysulfide Glassy Solid-State Electrolytes. *J. Electrochem. Soc.* **2023**, *170*, 110510.

(20) Kamaya, N.; Homma, K.; Yamakawa, Y.; Hirayama, M.; Kanno, R.; Yonemura, M.; Kamiyama, T.; Kato, Y.; Hama, S.; Kawamoto, K.; Mitsui, A. A Lithium Superionic Conductor. *Nat. Mater.* **2011**, *10*, 682−686.

(21) Hori, S.; Suzuki, K.; Hirayama, M.; Kato, Y.; Kanno, R. Lithium Superionic Conductor $Li_{9.42}Si_{1.02}P_{2.1}S_{9.96}O_{2.04}$ with $Li_{10}GeP_2S_{12}$-Type Structure in the Li_2S−P_2S_5−SiO_2 Pseudoternary System: Synthesis, Electrochemical Properties, and Structure−Composition Relationships. *Frontiers in Energy Research* **2016**, DOI: 10.3389/fenrg.2016.00038.

(22) Suzuki, K.; Sakuma, M.; Hori, S.; Nakazawa, T.; Nagao, M.; Yonemura, M.; Hirayama, M.; Kanno, R. Synthesis, Structure, and Electrochemical Properties of Crystalline Li−P−S−O Solid Electrolytes: Novel Lithium-Conducting Oxysulfides of $Li_{10}GeP_2S_{12}$ Family. *Solid State Ionics* **2016**, *288*, 229−234.

(23) Kim, K.-H.; Martin, S. W. Structures and Properties of Oxygen-Substituted $Li_{10}SiP_2S_{12-x}O_x$ Solid-State Electrolytes. *Chem. Mater.* **2019**, *31*, 3984−3991.

(24) Liu, G.; Xie, D.; Wang, X.; Yao, X.; Chen, S.; Xiao, R.; Li, H.; Xu, X. High Air-Stability and Superior Lithium Ion Conduction of $Li_{3+3x}P_{1-x}Zn_xS_{4-x}O_x$ by Aliovalent Substitution of ZnO for All-Solid-State Lithium Batteries. *Energy Storage Materials* **2019**, *17*, 266−274.

(25) Banerjee, S.; Zhang, X.; Wang, L. Motif-based design of an oxysulfide class of lithium superionic conductors: toward improved stability and record-high li-ion conductivity. *Chem. Mater.* **2019**, *31*, 7265−7276.

(26) Lazar, M.; Kmiec, S.; Joyce, A.; Martin, S. Investigations into reactions between sodium metal and $Na_3PS_{4-x}O_x$ solid-state electrolytes: enhanced stability of the Na_3PS_3O solid-state electrolyte. *Acs Applied Energy Materials* **2020**, *3*, 11559−11569.

(27) Chi, X.; Zhang, Y.; Hao, F.; Kmiec, S.; Dong, H.; Xu, R.; Zhao, K.; Ai, Q.; Terlier, T.; Wang, L.; et al. An electrochemically stable homogeneous glassy electrolyte formed at room temperature for all-solid-state sodium batteries. *Nat. Commun.* **2022**, *13*, 2854.

(28) Kmiec, S.; Olson, M.; Kenney, M.; Martin, S. W. Interpretation of the Na^+ Ionic Conductivity in $Na_4P_2S_{7-x}O_x$ Mixed Oxy-Sulfide Glasses: Effects of Oxygen Doping. *Chem. Mater.* **2022**, *34*, 9479−9491.

(29) Takayanagi, T.; Nasu, A.; Tsuji, F.; Motohashi, K.; Sakuda, A.; Tatsumisago, M.; Hayashi, A. Preparation and Characterization of $Na_{2.88}Sb_{0.88}W_{0.12}S_{4-x}O_x$ Solid Electrolyte. *Journal of the Ceramic Society of Japan* **2022**, *130*, 498−503.

(30) Kuwano, J.; West, A. New Li^+ ion conductors in the system, Li_4GeO_4−Li_3VO_4. *Mater. Res. Bull.* **1980**, *15*, 1661−1667.

(31) Hori, S.; Kato, M.; Suzuki, K.; Hirayama, M.; Kato, Y.; Kanno, R. Phase Diagram of the Li_4GeS_4−Li_3PS_4 Quasi-Binary System Containing the Superionic Conductor $Li_{10}GeP_2S_{12}$. *J. Am. Ceram. Soc.* **2015**, *98*, 3352−3360.

(32) Sun, Y.; Suzuki, K.; Hori, S.; Hirayama, M.; Kanno, R. Superionic conductors: $Li^{10+\delta}[Sn^ySi^{1-y}]^{1+\delta}P^{2-\delta}S^{12}$ with a $Li^{10}GeP^2S^{12}$-type Structure in the Li^3PS^4−Li^4SnS^4−Li^4SiS^4 quasi-ternary system. *Chem. Mater.* **2017**, *29*, 5858−5864.

(33) Muy, S.; Bachman, J. C.; Chang, H.-H.; Giordano, L.; Maglia, F.; Lupart, S.; Lamp, P.; Zeier, W. G.; Shao-Horn, Y. Lithium Conductivity and Meyer-Neldel Rule in Li^3PO^4−Li^3VO^4−Li^4GeO^4 Lithium Superionic Conductors. *Chem. Mater.* **2018**, *30*, 5573−5582.

(34) Zhao, G.; Suzuki, K.; Yonemura, M.; Hirayama, M.; Kanno, R. Enhancing fast lithium ion conduction in Li^4GeO^4−Li^3PO^4 solid electrolytes. *ACS Applied Energy Materials* **2019**, *2*, 6608−6615.

(35) Zhao, G.; Suzuki, K.; Seki, T.; Sun, X.; Hirayama, M.; Kanno, R. High lithium ionic conductivity of γ-Li3PO4-type solid electrolytes in Li^4GeO^4−Li^4SiO^4−Li^3VO^4 quasi-ternary system. *J. Solid State Chem.* **2020**, *292*, 121651.

(36) Zhang, L.; Malys, M.; Jamroz, J.; Krok, F.; Wrobel, W.; Hull, S.; Yan, H.; Abrahams, I. Structure and conductivity in LISICON analogues within the Li^4GeO^4−Li^2MoO^4 System. *Inorg. Chem.* **2023**, *62*, 11876−11886.

(37) Liu, Z.; Fu, W.; Payzant, E. A.; Yu, X.; Wu, Z.; Dudney, N. J.; Kiggans, J.; Hong, K.; Rondinone, A. J.; Liang, C. Anomalous High Ionic Conductivity of Nanoporous β-Li^3PS^4. *J. Am. Chem. Soc.* **2013**, *135*, 975−978.

(38) Hodge, I. M.; Ingram, M. D.; West, A. R. Ionic conductivity of Li^4SiO^4, Li^4GeO^4, and their solid solutions. *J. Am. Ceram. Soc.* **1976**, *59*, 360−366.

https://doi.org/10.1021/acs.chemmater.4c01267
Chem. Mater. XXXX, XXX, XXX−XXX

(39) Wang, C.; Liu, Z.-G.; Lin, P.-P.; Lu, F.-G.; Lin, J.-C.; Shi, Y.-H.; Xu, J.-J.; Xu, X.; Lin, T.-S.; Dong, Y.-K. A novel promotion strategy for microstructure and electrical performance of garnet electrolytes via Li^4GeO^4 additive. *Ceram. Int.* **2023**, *49*, 19905−19915.
(40) Homma, K.; Yonemura, M.; Kobayashi, T.; Nagao, M.; Hirayama, M.; Kanno, R. Crystal Structure and Phase Transitions of the Lithium Ionic Conductor Li^3PS^4. *Solid State Ionics* **2011**, *182*, 53−58.
(41) Lepley, N. D.; Holzwarth, N. A. W.; Du, Y. A. Structures, Li^+ Mobilities, and Interfacial Properties of Solid Electrolytes Li^3PS^4 and Li^3PO^4 from First Principles. *Phys. Rev. B* **2013**, *88*, 104103.
(42) Kaup, K.; Zhou, L.; Huq, A.; Nazar, L. F. Impact of the Li Substructure on the Diffusion Pathways in Alpha and Beta Li^3PS^4: An *in Situ* High Temperature Neutron Diffraction Study. *Journal of Materials Chemistry A* **2020**, *8*, 12446−12456.
(43) Völlenkle, H.; Wittmann, A. Die Kristallstruktur von Li^4GeO^4. *Zeitschrift für Kristallographie - Crystalline Materials* **1969**, *128*, 66−71.
(44) Dubey, B.; West, A. Crystal Chemistry of Li^4XO^4 Phases: X = Si, Ge, Ti. *Journal of Inorganic and Nuclear Chemistry* **1973**, *35*, 3713−3717.
(45) Hofmann, R.; Hoppe, R. Ein neues Oxogermanat: Li^8GeO^6 = $Li^8O^2[GeO^4]$. (Mit einer Bemerkung über Li^8SiO^6 und Li^4GeO^4). *Zeitschrift für anorganische und allgemeine Chemie* **1987**, *555*, 118−128.
(46) Rodger, A. R.; Kuwano, J.; West, A. R. Li^+ ion conducting *gamma* solid solutions in the systems Li^4XO^4−Li^3YO^4: X = Si, Ge, Ti; Y = P, As, V; Li^4XO^4−$LiZO^2$: Z = Al, Ga, Cr and Li^4GeO^4−Li^2CaGeO^4. *Solid State Ionics* **1985**, *15*, 185.
(47) Togo, A.; Chaput, L.; Tadano, T.; Tanaka, I. Implementation strategies in phonopy and phono3py. *J. Phys.: Condens. Matter* **2023**, *35*, 353001.
(48) Sanchez, J. M.; Ducastelle, F.; Gratias, D. Generalized cluster description of multicomponent systems. *Physica A: Statistical Mechanics and its Applications* **1984**, *128*, 334−350.
(49) Puchala, B.; Thomas, J. C.; Natarajan, A. R.; Goiri, J. G.; Behara, S. S.; Kaufman, J. L.; Van Der Ven, A. CASM − A Software Package for First-Principles Based Study of Multicomponent Crystalline Solids. *Comput. Mater. Sci.* **2023**, *217*, 111897.
(50) Deng, Z.; Sai Gautam, G.; Kolli, S. K.; Chotard, J.-N.; Cheetham, A. K.; Masquelier, C.; Canepa, P. Phase behavior in rhombohedral NaSiCON electrolytes and electrodes. *Chem. Mater.* **2020**, *32*, 7908−7920.
(51) Xie, F.; Zhong, P.; Barroso-Luque, L.; Ouyang, B.; Ceder, G. Semigrand-canonical Monte-Carlo simulation methods for charge-decorated cluster expansions. *Comput. Mater. Sci.* **2023**, *218*, 112000.
(52) Richards, W. D.; Miara, L. J.; Wang, Y.; Kim, J. C.; Ceder, G. Interface Stability in Solid-State Batteries. *Chem. Mater.* **2016**, *28*, 266−273.
(53) Xiao, Y.; Wang, Y.; Bo, S.-H.; Kim, J. C.; Miara, L. J.; Ceder, G. Understanding Interface Stability in Solid-State Batteries. *Nature Reviews Materials* **2020**, *5*, 105−126.
(54) Butler, K. T.; Sai Gautam, G.; Canepa, P. Designing Interfaces in Energy Materials Applications with First-Principles Calculations. *npj Computational Materials* **2019**, *5*, 19.
(55) Chen, T.; Ceder, G.; Sai Gautam, G.; Canepa, P. Evaluation of Mg Compounds as Coating Materials in Mg Batteries. *Frontiers in Chemistry* **2019**, DOI: 10.3389/fchem.2019.00024.
(56) Hellenbrandt, M. The Inorganic Crystal Structure Database (ICSD) − Present and Future. *Crystallography Reviews* **2004**, *10*, 17−22.
(57) Silberberg, M. S. *Principles of General Chemistry*, 2nd ed.; McGraw-Hill Education: New York, 2010.
(58) Tachez, M.; Malugani, J.; Mercier, R.; Robert, G. Ionic Conductivity of and Phase Transition in Lithium Thiophosphate Li3PS4. *Solid State Ionics* **1984**, *14*, 181−185.
(59) Forrester, F. N.; Quirk, J. A.; Famprikis, T.; Dawson, J. A. Disentangling cation and anion dynamics in Li^3PS^4 solid electrolytes. *Chem. Mater.* **2022**, *34*, 10561−10571.
(60) Zhang, Z.; Li, H.; Kaup, K.; Zhou, L.; Roy, P.-N.; Nazar, L. F. Targeting superionic conductivity by turning on anion rotation at room temperature in fast ion conductors. *Matter* **2020**, *2*, 1667−1684.
(61) Kuhn, A.; Duppel, V.; Lotsch, B. V. Tetragonal $Li^{10}GeP^2S^{12}$ and Li^7GePS^8 − Exploring the Li Ion Dynamics in LGPS Li Electrolytes. *Energy Environ. Sci.* **2013**, *6*, 3548.
(62) Kohn, W.; Sham, L. J. Self-Consistent Equations Including Exchange and Correlation Effects. *Phys. Rev.* **1965**, *140*, A1133−A1138.
(63) Kresse, G.; Furthmüller, J. Efficient iterative schemes for ab initio total-energy calculations using a plane-wave basis set. *Phys. Rev. B* **1996**, *54*, 11169−11186.
(64) Kresse, G.; Joubert, D. From ultrasoft pseudopotentials to the projector augmented-wave method. *Phys. Rev. B* **1999**, *59*, 1758−1775.
(65) Blochl, P. E. Projector augmented-wave method. *Phys. Rev. B* **1994**, *50*, 17953−17979.
(66) Sun, J.; Ruzsinszky, A.; Perdew, J. P. Strongly Constrained and Appropriately Normed Semilocal Density Functional. *Phys. Rev. Lett.* **2015**, *115*, No. 036402.
(67) Ong, S. P.; Richards, W. D.; Jain, A.; Hautier, G.; Kocher, M.; Cholia, S.; Gunter, D.; Chevrier, V. L.; Persson, K. A.; Ceder, G. Python Materials Genomics (pymatgen): A robust, open-source python library for materials analysis. *Comput. Mater. Sci.* **2013**, *68*, 314−319.
(68) Nosé, S. A unified formulation of the constant temperature molecular dynamics methods. *J. Chem. Phys.* **1984**, *81*, 511−519.
(69) Hoover, W. G. Canonical dynamics: Equilibrium phase-space distributions. *Phys. Rev. A* **1985**, *31*, 1695.
(70) Perdew, J. P.; Burke, K.; Ernzerhof, M. Generalized gradient approximation made simple. *Physical review letters* **1996**, *77*, 3865−3868.

https://doi.org/10.1021/acs.chemmater.4c01267
Chem. Mater. XXXX, XXX, XXX−XXX